Monthly Notices of the ROYAL ASTRONOMICAL SOCIETY

MNRAS **503,** 4719–4733 (2021) doi:10.1093/mnras/stab857
Advance Access publication 2021 March 25

Metallicities from high-resolution spectra of 49 RR Lyrae variables

Christina K. Gilligan [1]★ Brian Chaboyer,[1] Massimo Marengo,[2] Joseph P. Mullen,[2] Giuseppe Bono,[3,4] Vittorio F. Braga [3,5] Juliana Crestani,[3,4] Massimo Dall'Ora,[6] Giuliana Fiorentino,[3] Matteo Monelli [7] Jill R. Neeley [8] Michele Fabrizio,[3,5] Clara E. Martínez-Vázquez [9] Frédéric Thévenin [10] and Christopher Sneden[11]

[1]*Department of Physics and Astronomy, Dartmouth College, Hanover, NH 03784, USA*
[2]*Department of Physics and Astronomy, Iowa State University, Ames, IA 50011, USA*
[3]*INAF-Osservatorio Astronomico di Roma, via Frascati 33, I-00078 Monte Porzio Catone, Italy*
[4]*Dipartimento di Fisica, Università di Roma Tor Vergata, via della Ricerca Scientifica 1, I-00133 Roma, Italy*
[5]*Space Science Data Center, via del Politecnico snc, I-00133 Roma, Italy*
[6]*INAF-Osservatorio Astronomico di Capodimonte, Salita Moiariello 16, I-80131 Napoli, Italy*
[7]*Instituto de Astrofísica de Canarias, Calle Via Lactea s/n, E-38205 La Laguna, Tenerife, Spain*
[8]*Department of Physics, Florida Atlantic University, 777 Glades Road, Boca Raton, FL 33431, USA*
[9]*Cerro Tololo Inter-American Observatory, NSF's NOIRLab, Casilla 603, La Serena, Chile*
[10]*Université de Nice Sophia-antipolis, CNRS, Observatoire de la Côte d'Azur, Laboratoire Lagrange, BP 4229, F-06304 Nice, France*
[11]*Department of Astronomy and McDonald Observatory, The University of Texas, Austin, TX 78712, USA*

Accepted 2021 March 17. Received 2021 March 17; in original form 2020 August 24

ABSTRACT

Accurate metallicities of RR Lyrae are extremely important in constraining period–luminosity–metallicity (*PLZ*) relationships, particularly in the near-infrared. We analyse 69 high-resolution spectra of Galactic RR Lyrae stars from the Southern African Large Telescope. We measure metallicities of 58 of these RR Lyrae stars with typical uncertainties of 0.15 dex. All but one RR Lyrae in this sample has accurate ($\sigma_{\varpi} \lesssim 10$ per cent) parallax from *Gaia*. Combining these new high-resolution spectroscopic abundances with similar determinations from the literature for 93 stars, we present new *PLZ* relationships in WISE $W1$ and $W2$ magnitudes, and the Wesenheit magnitudes $W(W1, V-W1)$ and $W(W2, V-W2)$.

Key words: stars: abundances – stars: variables: RR Lyrae.

1 INTRODUCTION

H_0 is one of the most important cosmological parameters in Lambda cold dark matter (ΛCDM) models. However, there is disagreement on the precise value of H_0. Measurements using early-time features (CMB, BAO, etc.) find a value of $H_0 = 67.5 \pm 0.5$ km s^{-1} Mpc^{-1} (Planck Collaboration VI 2018), while the most precise measurements using the cosmic distance ladder that is a local measurement of H_0, usually based upon Cepheids and SNeIa, find $H_0 = 74.03 \pm 1.42$ km s^{-1} Mpc^{-1} (Riess et al. 2019). The difference in the early and late measurements of H_0 is over 4σ and this difference is increasingly thought to not be due to systematics. In order to determine whether the cause is due to physics outside of ΛCDM rather than systematics in the measurements, different calibrators for the cosmic distance ladder need to be examined. We use the cosmic distance ladder to determine extragalactic distances. First, distances to close objects are calibrated using geometrical methods and then used to calibrate farther objects, usually SNeIa. This succession of methods is called the distance ladder. Since each subsequent rung of the distance ladder relies on the rungs that come before, changing the first rung distance of the distance ladder has the largest impact.

RR Lyrae can be used as one of the first rungs of the cosmic distance ladder to get an independent measure of H_0. Cepheids have been preferred since they are more massive and therefore more luminous than RR Lyrae. However, RR Lyrae stars have a number of advantages over Cepheids as distant indicators. As younger stars, Cepheids are not found in early-type galaxies, and are often located in the actively star-forming regions of galaxies, which can lead to large extinctions and reddening. In contrast the older, lower mass RR Lyrae stars are present in all types of galaxies, and can be found in regions with little or no extinction.

Another benefit of RR Lyrae is their lower luminosity dispersion as compared to Cepheids (Bono 2003), which implies that the uncertainties in the RR Lyrae period–luminosity–metallicity relationship will be smaller than those for Cepheids. We note that a period–luminosity–metallicity relationship for RR Lyrae only exists in the infrared bands. Finally, RR Lyrae stars are much more common than Cepheid stars. However, RR Lyrae stars are still relatively rare, and until the advent of *Gaia*, there were few accurate parallaxes for them. Benedict et al. (2011) measured the parallaxes of five RR Lyrae using the *Hubble Space Telescope* (*HST*), the largest sample at that time. Fortunately, *Gaia* has measured the parallaxes of thousands of RR Lyrae (Gaia Collaboration 2018a) and even better parallaxes are expected soon with the third Data Release.

The most popular diagnostic to estimate the distances of individual RR Lyrae has been for decades the use of the visual magnitude–

★ E-mail: christinagilligan@gmail.com

metallicity relation (M_V versus [Fe/H]). However, this relation is prone to several thorny problems. First, evolved RR Lyrae appear systematically brighter in the M_V,[Fe/H] plane and we do not have firm constraints on the evolutionary status of individual stars, as we lack solid estimates for the surface gravity of individual RR Lyrae stars. Secondly, the M_V–[Fe/H] may not be linear over the entire metallicity range (e.g. Catelan, Pritzl & Smith 2004; Marconi et al. 2015). Thirdly, the steep dependence of M_V on [Fe/H] implies that uncertainties in the metallicities (either in individual estimates or the adopted metallicity scale) has a significant impact on the derived distances. An error of $\sim$0.2−0.3 dex in the metallicity estimate implies an error on the absolute visual magnitude of $\sim$0.06−0.10 mag. Finally, reddening corrections are important in the visual; error of $\approx$ 0.02 mag in the reddening correction implies an error of $\approx$ 0.06 mag in the derived distance modulus.

A significant fraction of the pitfalls affecting the visual magnitude–metallicity relation can be either avoided or limited when moving into the mid-infrared (3–5 μm) regime. Dating back to Longmore, Fernley & Jameson (1986), it becomes clear that RR Lyrae obey a well-defined period–luminosity relation in the near-infrared bands (e.g. see Braga et al. 2018, for a more recent discussion), and the same is true in the mid-infrared (e.g. Neeley et al. 2017; Muraveva et al. 2018b; Neeley et al. 2019), There are two key advantages in using mid-infrared period–luminosity relations: the slope becomes systematically steeper when moving from the I to the K band and at the same time the standard deviation becomes smaller. Theoretical calculations indicate that the mid-infrared period–luminosity relations are minimally affected by evolutionary effects and that they are linear over the entire period range (Neeley et al. 2017). Moreover and even more importantly, fundamental and first-overtone RR Lyrae obey independent period luminosity relations. Finally, absorption in the mid-infrared is more than order of magnitude less than in the visual, with a corresponding decrease in the uncertainty related to absorption corrections. Current theoretical (Neeley et al. 2017) and empirical (Neeley et al. 2019) evidence indicates that the mid-infrared period–luminosity relation depends on the metal content, but the coefficient of the metallicity term is typically smaller than $\sim$0.15 dex. In this context, it is worth mentioning that individual distances based on *Gaia* DR2 trigonometric parallaxes agree quite well, within the errors, with theoretical predictions (Muraveva et al. 2018b). Another motivation to use period–luminosity relations in the mid-infrared is that JWST/NIRCAM will have a high sensitivity at these wavelengths, leading to the possibility of obtaining RR Lyrae distances to a number of different galaxies.

Once the systematics of *Gaia* parallaxes are fully understood, the main source of uncertainty in using RR Lyrae as a standardizable candle will be the metallicity coefficient of the period–luminosity–metallicity (*PLZ*). Measuring metallicities of RR Lyrae is commonly performed using three methods: the ΔS method (from low-resolution spectra), photometric metallicities through colours and shapes of the light curves, and directly through high-resolution spectroscopy (HRS). The former two methods typically rely upon the use of calibration stars with known metallicities to establish empirical relations that are used to convert a ΔS measurement, or light-curve shape measurement into a metallicity. In contrast, HRS provides a direct measurement of the metallicity.

The number of HRS metallicities of RR Lyrae from HRS has always trailed those of Cepheids and other variable stars. The periods of RR Lyrae are fairly short, almost always less than 0.9 d, making long exposures useless due to the cyclical velocity smearing. In addition, RR Lyrae stars span a wide range of metallicities, ranging from $\sim$−3.0 (Govea et al. 2014) to $\sim$0.1 dex (Chadid, Sneden & Preston 2017), implying that a large variety of spectral lines need to be measured in order to find lines useful for metallicity determinations.

At present, there are 105 RR Lyrae with metallicities determined from HRS (Fabrizio et al. 2019) and an additional 23 stars from Liu et al. (2013) with a [Fe/H] spread of $\sim$2.5 dex. This work aims to significantly expand the number of RR Lyrae with accurate metallicities by presenting 49 new metallicity measurements of RR Lyrae.

The long-term goal is to create a large, homogeneous data set to more precisely and accurately determine the near-infrared $PL_{J,H,K}Z$ relationships in order to independently determine H_0. We have also obtained at least 20 epochs of near-infrared (*JHK*) photometry for all of the stars examined in this work. Dall'Ora et al. (in preparation) will analyse the photometry and present near-infrared light curves for these stars.

We present our observations and data reduction in Section 2. We then explain our stellar parameter fitting routine in Section 3. We compare the results we obtain with this routine for previously fit spectra in addition to comparing our metallicity results to previous measurements in Section 4. In Section 5, we use these newly measured metallicities to create new $PL_{W1,W2,W}Z$ relationships. Section 6 contains our final conclusions and remarks.

2 OBSERVATIONS AND DATA REDUCTION

2.1 Target selection

All of our target stars are present in the *Gaia* DR2 catalogue with positive parallaxes with uncertainties less than 10 per cent. We prioritized stars present in the Chadid et al. (2017) sample to be able to directly compare our work with previous studies. In addition, seven stars were observed twice in order to validate the internal consistency of our analysis programme. Priority is given to stars for which we have collected a full light curve in the near-infrared. The stars are listed in Table 1.

2.2 Data

Observations were performed with HRS on the Southern African Large Telescope (SALT). HRS is a dual beam (3700–5500 and 5500–8900 Å) echelle spectrograph. We used the medium resolution mode with $R \sim 37\,000$. SALT is a queue observed telescope and allows for objects to be observed only at certain epochs if the ephemeris data are provided. Exposure times were chosen such that the S/N of the spectra was $\sim$100 accounting for various weather conditions and estimated luminosity based on pulsation period and phase. However, as discussed in Section 3, after recent refinement of the periods, we found that the phase of our observations was significantly different than what was initially thought so some spectra had worse S/N (with a lower limit of 40) and some had higher with an average S/N of 115. A number of studies have suggested that reliable [Fe/H] abundances are best determined in the range of phases $\sim$0.2–0.5 (e.g. For, Sneden & Preston 2011; Preston 2011; Chadid et al. 2017) as in these phases it is thought that the RR Lyrae atmospheres are relatively quiet, without shocks or significant velocity gradients. Thus, the fact that our spectra were obtained at practical random phase is not ideal. However, detailed studies have shown that the derived [Fe/H] abundances do not show a significant dependence on the observed phase (e.g. For et al. 2011;

Table 1. Stars observed. Full table available as supplementary material.

Name	*Gaia* EDR3 ID	ϖ (mas)	σ_{ϖ} (mas)	Period (d)	T_0[a] (HJD)	Obs (HJD)	Phase	Type
AA Aql	4224859720193721856	0.720 56	0.017 85	0.361 786 0175	2457194.01212	2458618.591308	0.63	ab
AA CMi	3111925220109675136	0.871 77	0.017 75	0.476 326 4561	2457305.072	2458063.564907	0.38	ab
AE Scl	5027734380789950976	0.397 06	0.020 37	0.550 131 4496	2457277.87304	2458296.599236	0.22	ab
AE Scl	5027734380789950976	0.397 06	0.020 37	0.550 131 4496	2457277.87304	2458074.444962	0.79	ab
AE Tuc	4710156463040888192	0.579 36	0.014 05	0.414 5285	2434273.232	2458275.647141	0.93	ab

[a] T_0 is the time of minimum light.

Fossati et al. 2014), and so we analysed all of our spectra, regardless of the observed phase. We return to this issue Sections 3.2 and 4.1.

The data are first reduced using the MIDAS (Kniazev, Gvaramadze & Berdnikov 2016, 2017) pipeline, designed to be used for SALT spectra. MIDAS performs flat, arc, and object reductions, outputting a one-dimensional spectra. The MIDAS pipeline has some difficulties removing the echelle blaze pattern of the spectrograph, which is true for nearly all echelle pipelines. In order to lessen this effect, we fit a second-order polynomial to each order of the spectrum, ignoring all features that are over 3σ from the fit. We then straighten the spectrum along this polynomial. In addition, there a number of areas of the spectra that are much noisier than the rest of the spectrum. We masked these bad areas of the spectrum. Luckily, these areas are fairly constant in placement on the CCD, so the same mask is applied to all of our spectra. This procedure is illustrated for a single echelle order in Fig. 1. Not including the masks does not greatly affect the results of our stellar parameter fitting program, but does add uncertainty to our fits.

3 DATA ANALYSIS

The [Fe/H] abundances are determined using a synthetic spectral analysis. This method takes a model atmosphere with set input stellar parameters along with a line list and outputs a synthetic spectra that we can then compare to our SALT spectra. We create synthetic spectra using the synth driver of the LTE code MOOG[1] (Sneden 1973; Sobeck et al. 2011), which can then be compared to our observed spectra.

The power of our fitting procedure is that we are able to fit the entire spectra at once, from around 4000 to 7500 Å using an extremely large grid of stellar atmosphere models. The overall outline of our fitting procedure is as follows: (1) refine the line list; (2) create the grid of atmosphere models and synthetic spectra; (3) find the instantaneous stellar radial velocity and the spectral line Gaussian smoothing parameters; (4) calculate χ^2 between the model and spectra; (5) recheck velocity and Gaussian smoothing parameters; and (6) if either the velocity or Gaussian smoothing parameters have changed, re-run comparison to models for models close in parameter space to the best-fitting model.

This automated method of determining [Fe/H] abundances was originally used as we had obtained a large number of spectra, many of which had lower signal to noise. However, in the end our automated method did not converge for the lower signal-to-noise spectra, so the data presented in this paper all have relatively high signal to noise ($\gtrsim 50$).

3.1 Linelist creation

The linelists are generated using the linemake code[2] which includes both hydrides and molecules. In order to get the most accurate line list possible, every line in our wavelength region (4000–7500 Å) has its oscillator strength ($\log gf$) adjusted to best match the spectrum of the Sun. Molecular lines play little role in determining the metallicity of these warm stars.

3.2 Creating atmosphere models

We used Kurucz stellar atmosphere models (Castelli & Kurucz 2004), with a fine grid of stellar parameters. Our choice of parameters are shown in Table 2. In total, we create over 230 000 stellar atmosphere models, each of which is compared to all of our spectra.

3.3 Synthetic spectral analysis

In order to directly compare our SALT spectra to the synthetic spectra created by MOOG, we need to shift our spectra in velocity space. In addition, we need to degrade our synthetic spectra by a Gaussian smoothing parameter to match the instrumental spectral resolution. Both of these parameters are initially determined at the beginning of the fitting procedure with an test synthetic spectrum that is in the middle of our parameter space. After an initial best-fitting set of models is found, the velocity and Gaussian smoothing parameters are re-fitted to refine the validity of the initial values.

To find the best-fitting models, our programme finds the minimum χ^2 value between the grid of synthetic models and the SALT spectrum. For a number of stars, the χ^2 values have a very shallow minimum, making it impossible to determine an accurate metallicity for these stars. These stars are removed from our sample of [Fe/H] measurements. Stars that are removed are ones in which $\chi^2 = 1.1\chi^2_{\rm min}$ has a [Fe/H] value that is more than 0.25 dex away from the best-fitting model's [Fe/H]. In essence, for these spectra, our fitting procedure does not discriminate between a wide range of [Fe/H] values. Fig. 2 shows an example for two different stars, AA CMi and AT Vir. AA CMi has a well-determined [Fe/H] but AT Vir does not. The 11 removed stars are marked with an asterisk in Table 3. As discussed in Section 4.1, the stars for which we are unable to determine a reliable [Fe/H] value were all observed at phases >0.5, where the atmospheres are likely more turbulent, and hence appear not to be well characterized by one-dimensional hydrostatic atmosphere models.

[1] The current version is available at http://www.as.utexas.edu/~chris/moog.html.

[2] Downloaded from https://github.com/vmplacco/linemake and references therein.

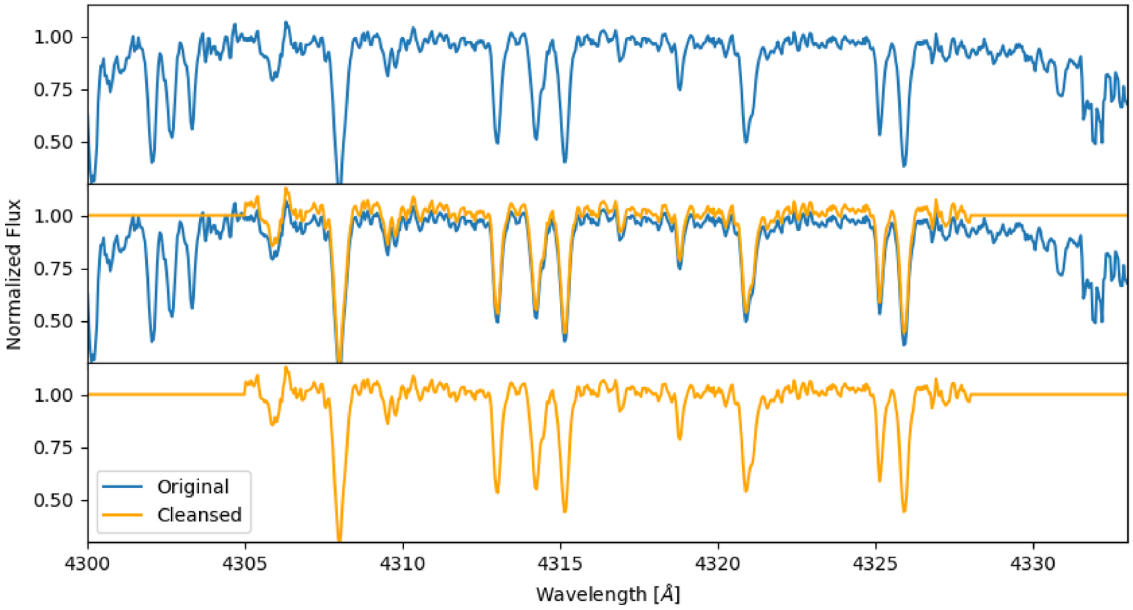

Figure 1. Polynomial subtraction and masking for an example star, SX For. At the ends of the order, the MIDAS pipeline output is much noisier than the middle of the order. We are conservative in masking noisy regions, but changing the masked regions has very little impact in our metallicity determinations.

Table 2. Parameter space of our Kurucz stellar models.

Parameter	Range	Step
T (K)	5000–8000	50
$\log g$ (dex)	1.0–3.0	0.25
Microturbulent velocity (ξ) (km s^{-1})	2.0–4.0	0.25
[Fe/H] (dex)	−3.00 to 0.00	0.05

3.4 Validation of our procedure

To validate our procedure, we fit the reduced spectra from Chadid et al. (2017) with our automated programme to determine [Fe/H], comparing the output stellar parameters with what was found by Chadid et al. (2017) who performed a synthetic spectral analysis by hand. These reduced spectra from Chadid et al. (2017) are entirely independent of our SALT spectra, and do not have stars in common. Since many of the stars Chadid et al. (2017) were also examined in Layden (1994), we can directly compare our metallicity measurements to literature values from both Chadid et al. (2017) and Layden (1994).

Fig. 3 compares [Fe/H] values found using our procedure ([Fe/H]$_G$) to the measurements from Chadid et al. (2017) ([Fe/H]$_C$). We removed stars that have poor metallicity determinations. After we remove these stars, we are left with 20 stars. The median difference is 0.09 dex with a standard deviation of 0.08 dex. There does not seem to be a trend with [Fe/H]. When directly comparing our best-fitting stellar parameters to those found in Chadid et al. (2017), our temperatures are nearly consistently 200–300 K hotter than in Chadid et al. (2017), which at least partially explains the [Fe/H] offset since the two parameters are correlated.

Fig. 4 is similar to Fig. 3 but instead compares our measured [Fe/H] ([Fe/H]$_G$) to the metallicities found in Layden (1994) ([Fe/H]$_L$). These are the same set of 20 stars in both Figs 3 and 4. The median difference is −0.06 dex with a standard deviation of 0.18 dex, mainly due to the large outlier at [Fe/H]$_G$ = −1.80 dex, VY Ser. Layden (1994) found a [Fe/H] = −1.29 dex while Chadid et al. (2017) found a [Fe/H] = −1.86 for this star, closer to the value that we find in this work. If this outlier is removed from the comparison to the Layden (1994) sample, the median difference is 0.04 dex with a standard deviation of 0.15 dex.

4 RESULTS

The Bailey diagram for our is shown in Fig. 5. The RRc stars are well distinguished from the RRab. Table 3 shows the best-fitting stellar parameters for our SALT spectra. It should be noted that varying the $\log g$ and ξ parameters do not greatly affect the final metallicity determination. Hence, their values are not well determined.

4.1 Comparison to literature values

The subset of the SALT spectra that contain well-observed Ca H and K lines are also analysed in Crestani et al. (2020) who present a new calibration of the ΔS method for abundance determination. They perform a conventional line-by-line abundance analysis that we can directly compare to our pipeline results since the spectra are the same. Fig. 6 shows the residuals between Crestani et al. (2020) and our analysis. Overall, there is good agreement between the two analysis methods. We also found that there was no correlation between the residuals and phase of observation. We can use the differences between the [Fe/H] values to estimate the error in our [Fe/H] determinations. We calculated the root mean square between the two samples and then use the quoted errors from Crestani et al. (2020) to determine our error. The error in our [Fe/H] determination is 0.15 dex.

Fabrizio et al. (2019) collected ∼2400 different metallicity measurements of RR Lyrae. Some of these stars (∼300) only have metallicity measurements from Dambis et al. (2013), which is based upon the catalogue from Beers et al. (2000), which mainly used HK objective prism spectra, or medium resolution (R ∼ 4000) spectra to determine metallicities. A smaller sample of ∼100 stars instead have [Fe/H] abundances derived from HRS. For all other stars, Fabrizio et al. (2019) derived metallicities using the ΔS method for spectra with R ∼2000. Fig. 7 shows the comparison between our

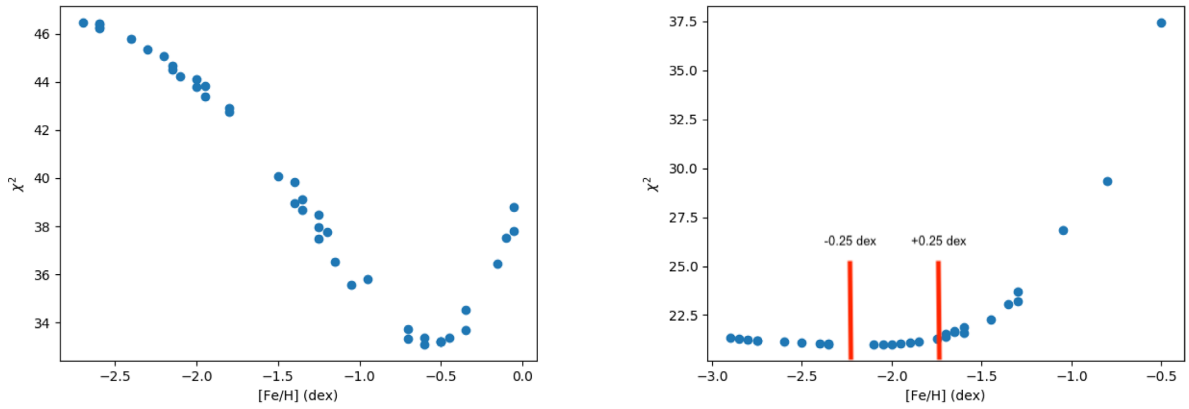

(a) (b)

Figure 2. Two example fitting results. They are for the best-fitting temperature, log g, and microturbulent velocity (ξ). Panel (a) shows the results for AA CMi. It is clear that our procedure is able to determine a best-fitting well. Panel (b) shows the results for AT Vir. It is clear that the fitting does not discriminate well between [Fe/H] values.

Table 3. Fitted stellar parameters of our RR Lyrae. Full table available as supplementary material. The estimated uncertainty in our [Fe/H] values is $\sigma_{[Fe/H]} = 0.15$ dex.

Name	[Fe/H]	Temperature (K)	log g (dex)	ξ (km s^{-1})
AA Aql[a]	− 1.25	6400	2.75	3.00
AA CMi	− 0.6	6800	2.25	3.00
AE Scl	− 2.00	6700	2.75	3.00
AE Scl	− 1.70	6800	2.5	3.00
AE Tuc[a]	− 1.45	6800	2.75	3.00
AF Vel	− 1.60	6800	2.75	3.00

[a]Poor metallicity determination.

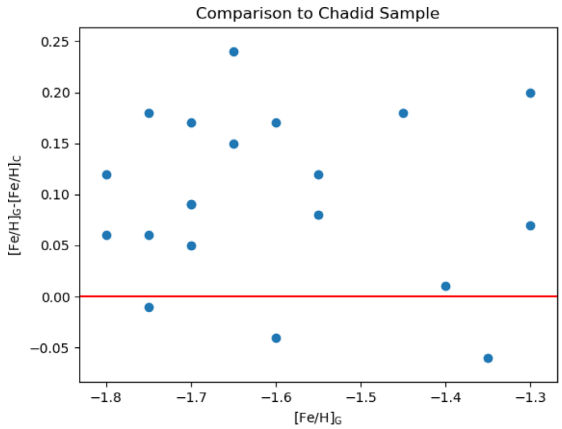

Figure 3. Comparison between the difference of [Fe/H] values found in this work ([Fe/H]$_G$) and those found in Chadid et al. (2017) ([Fe/H]$_C$).

measured metallicities and those collected in Fabrizio et al. (2019). The blue points only have measurements from Dambis et al. (2013). The red points are RR Lyrae that have metallicity measurements from both Dambis et al. (2013) and high-resolution spectroscopy. The median differences and standard deviations between our [Fe/H] and those with previous HRS is −0.14 and 0.21 dex (10 stars), while for the entire sample is −0.12 and 0.41 dex (36 stars), respectively. If we remove the two largest outliers ([Fe/H] ∼ −1.2 and −0.2 dex), the median and standard deviations become −0.10 and 0.19 dex.

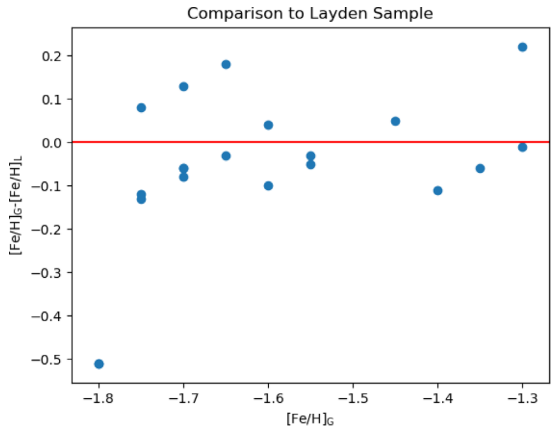

Figure 4. Comparison between the difference of [Fe/H] values found in this work ([Fe/H]$_G$) and those found in Layden (1994) ([Fe/H]$_L$).

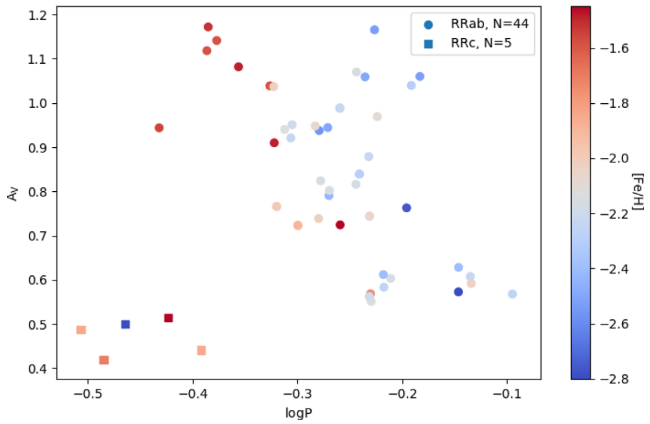

Figure 5. Bailey diagram for the stars for which we are able to find a best-fitting metallicity. The colours of the points correspond to the metallicity found in this work. The shapes indicate if the star is RRab or RRc.

Fig. 8 is similar to Fig. 7 but plot our residuals as a function of S/N and phase. There does not seem to be a correlation between our residual and S/N. However, while we are always able to obtain a reliable [Fe/H] estimate when the phase is less than ∼0.5, the

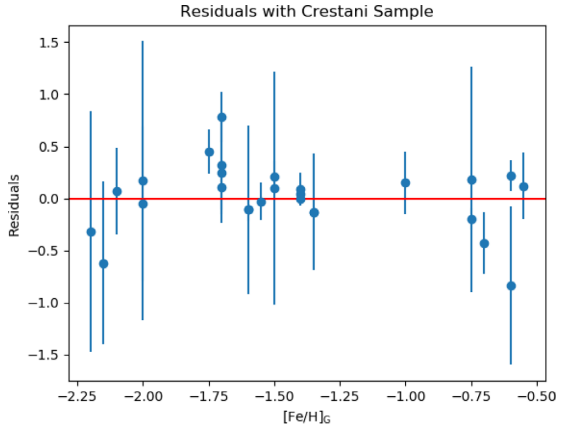

Figure 6. Comparison between the difference of [Fe/H] values found in this work ($[Fe/H]_G$) and those found by Crestani et al. (2020) ($[Fe/H]_C$). The error bars are only shown on the y-axis for clarity. There are 27 stars in common between the two independent analysis.

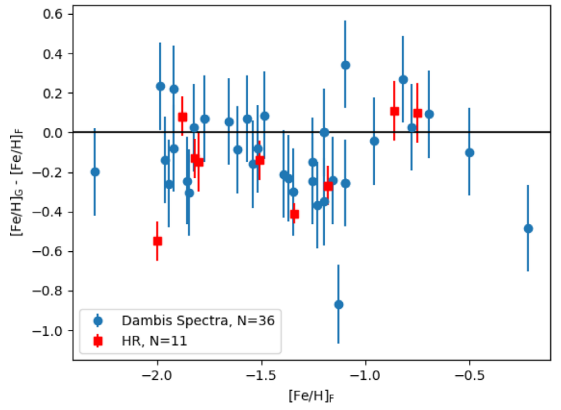

Figure 7. Comparison between the difference of [Fe/H] values found in this work ($[Fe/H]_G$) and those found collected in Fabrizio et al. (2019) ($[Fe/H]_F$). The median difference between the two samples from HR is −0.14 dex while for the Dambis et al. (2013) spectra alone is −0.12 dex. The error bars are only shown on the y-axis for clarity.

fitting procedure often fails at higher phases, when the atmosphere is more turbulent. Interesting enough, we are able to get reliable [Fe/H] abundances for many stars at phases >0.5, though the dispersion between our [Fe/H] abundances and those found in the literature increases at the higher phases.

Fig. 9 shows a histogram of our measured metallicities. There is a Fe rich tail (AA CMi, AL CMi, SS Tau, U Pic, W Crt). Since we chose stars that were bright enough to be observed with short exposure times, we are biased towards stars close to the Sun and therefore of more similar Fe abundances to the Sun. In addition, it is easier to determine metallicities for more metal-rich stars since the Fe lines are more apparent.

5 PERIOD–LUMINOSITY–METALLICITY RELATIONSHIPS

Our newly determined metallicities were combined with high-dispersion spectroscopic abundance determinations from the literature to come up with a sample of RR Lyr stars that have had their [Fe/H] values determined directly from high-quality spectra. Periods and mean magnitudes of this sample were taken from Mullen et al. (2020) to compute new *PLZ* relationships. This paper utilizes near-infrared photometry from both the Wide-field Infrared Survey Explorer (WISE) (Wright et al. 2010) and its reactivation, the Near-Earth Object Wide-field Infrared Survey Explorer Reactivation Mission (NEOWISE) (Mainzer et al. 2011) in the 3.4 and 4.6 μm bands, $W1$ and $W2$, respectively. Visible time-series photometric measurements, in the V band, were taken from the All-Sky Automated Survey for Supernovae (ASAS-SN) (Shappee et al. 2014; Jayasinghe et al. 2018).

Periods are recalculated using the Lomb–Scargle method on both the V and $W1$ band data. The long survey length of the combined WISE and NEOWISE mission, running from late 2009 to present, allows us to define a well-defined periods with accuracy on the order of 10^{-6} d or greater to properly phase without any drifting. Mean magnitudes for each band were determined by fitting the phased light curves with a Gaussian locally weighted regression smoother (GLOESS) algorithm to gain a smoothed light curve. From the GLOESS light curves, characteristics such as amplitude, time of minimum light (T_0), and mean magnitude with its error can be easily calculated. For instance, the measurement of T_0 is defined as the epoch that lies closest in phase to the GLOESS smoothed light-curve minimum.

There are 120 stars that have data for both surveys and high-quality light-curve fits. Out of these 120 stars, the max period difference between ASAS-SN and NEOWISE is 0.002 d, with 114 of these 120 star have period differences on the order of 10^{-5} d or smaller. The median period difference is 1.02×10^{-5} d, and we assume an uncertainty of 10^{-5} d in the period when performing our *PLZ* fits. For a more detailed description of the NEOWISE, ASAS-SN survey, light-curve processing, various quality checks, and data extraction, we refer you to Mullen et al. (2020). For specific reading on the GLOESS algorithm or the calculation of mean magnitude from a GLOESS light curve, please read Persson et al. (2004) or Neeley et al. (2015), respectively.

The final sample contains 138 stars that have well-determined periods, *Gaia* EDR3 parallaxes (Fabricius et al. 2020; Lindegren et al. 2020b), $W1$ magnitudes, and [Fe/H] values. To avoid biases that result from selecting a sample based upon parallax quality (e.g. removing negative parallaxes), the astrometric based luminosity (ABL) prescription (Arenou & Luri 1999) was used to determine the *PLZ* relations for these stars.

The *PLZ* relation was fitted using the following equation:

$$\varpi 10^{0.2m_o-2} = 10^{0.2[a(\log P+0.27)+b([Fe/H]+1.3)+c]}, \quad (1)$$

where ϖ is the EDR3 parallax in mas, m_o is the absorption corrected apparent magnitude, and the coefficients a, b, and c are determined as part of the fit process. This explicit, non-linear fit, which takes into account the uncertainties in all of the observed quantities was performed using R (R Core Team 2018) and its non-linear fitting function `nls`. In performing these fits, the uncertainty in the EDR3 parallaxes have been increased, based upon section 7.1.2 of the EDR3 documentation[3] and fig. 19 in Fabricius et al. (2020). In addition, an intrinsic dispersion of 0.03 mag was assumed to exist in the *PLZ* relation.

Considerable effort was put into reducing the systematic parallax uncertainties in EDR3. However, the Gaia collaboration believes that there are still systematic parallax uncertainties that are a function

[3]https://gea.esac.esa.int/archive/documentation/GEDR3/Catalogue_consolidation/chap_cu9val/sec_cu9val_introduction/ssec_cu9val_intro_astro_precision.html

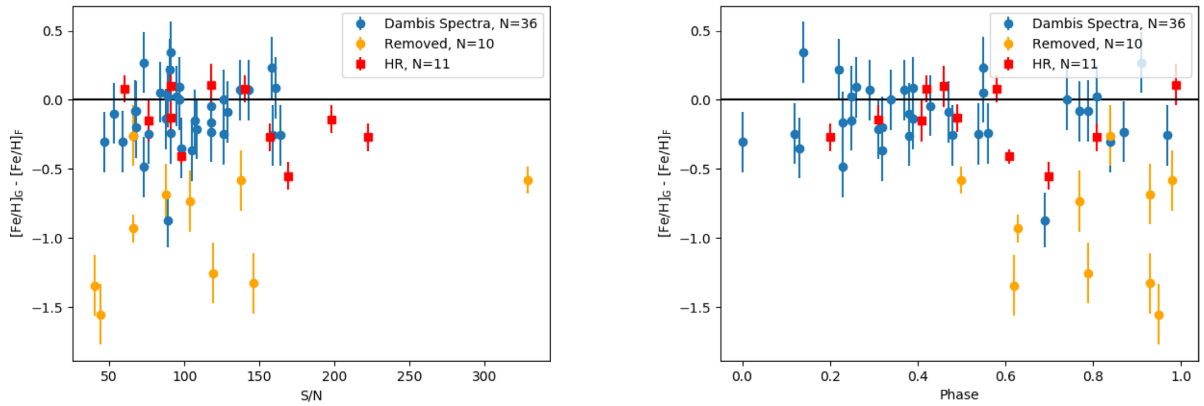

Figure 8. Comparison between the difference of [Fe/H] values found in this work ([Fe/H]$_G$) and those collected in Fabrizio et al. (2019) ([Fe/H]$_F$). The left-hand panel compares the fits with S/N while the right compares with phase. The removed stars are ones where the fitting procedure is unable to distinguish a best-fitting metallicity. There does not seem to be a trend with respect to S/N. However, it is clear that closer to minimum light (phase = 1), it is more difficult for our routine to find a best-fitting metallicity. For an RRab, the luminosity rises quickly after the minimum light which is likely why metallicities between a phase of 0–0.2 are easier to determine.

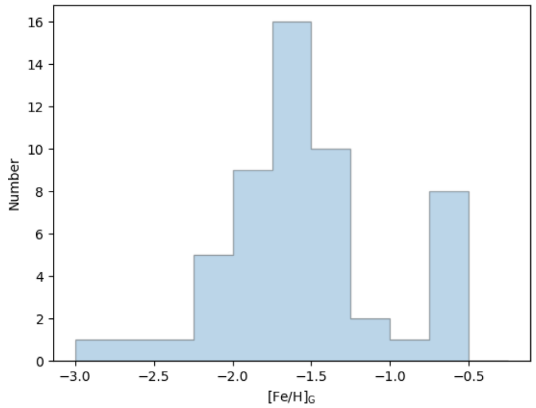

Figure 9. Histogram of our measured metallicities ([Fe/H]$_G$). The shape is relatively Gaussian with a secondary peak of stars with an [Fe/H] between −0.75 and -0.5 dex. Due to the small number of stars examined and the fact that it is more difficult to measure metallicities for stars which have weak Fe lines, it is not unexpected to have this kind of population. In addition, since we chose our stars by apparent magnitude, we are biased towards RR Lyrae that are close to the Sun. Note that there is no physical reason why the metallicity distribution should be Gaussian. Apart from low number statistics and various biases, the distribution should reflect the overall [Fe/H] distribution in the halo.

of magnitude, colour, position on the sky and astrometric solution type, and have published a calibration of this error (Lindegren et al. 2020a). We have applied this zero-point correction when performing the explicit *PLZ* fits.

EDR3 contains a number of astrometric quality indicators, including the reduced uniform weight error, RUWE, and it is recommended that stars with RUWE <1.4 be used when one desires to reduce the number of spurious parallaxes (Fabricius et al. 2020). From our original sample of 138 stars, 114 have RUWE <1.4 and were used in an initial *PLZ* fit in the *W*1 filter. This resulted in a very poor fit, mainly due to the inclusion of RR Lyr, which is a significant 4.5 σ outlier from the fit. To determine possible reasons why RR Lyr was an outlier, other astrometric goodness of fits indicators in EDR3 were examined: `astrometric_excess_noise`, `ipd_gof_harmonic_amplitude`, `ipd_frac_multi_peak`, and `ipd_frac_odd_win`. RR Lyr, along with a few other stars appears as an outlier in this sample, with relatively large `astrometric_excess_noise`. In addition, some stars were outliers with relatively large values of `ipd_gof_harmonic_amplitude`, which is an indication of asymmetric images. To remove these potential astrometric outliers, we required `astrometric_excess_noise` <0.23 and `ipd_gof_harmonic_amplitude` <0.25, which resulted in a sample of 108 stars that are used in the *PLZ* fits. There are five RRc stars in this sample, with the rest of the sample being RRab stars. In performing the *PLZ* fits, the periods of the RRc stars were fundamentalized by adding 0.127 to log *P*. The relevant data for these 108 stars are given in Table 4.

SALT [Fe/H] values were available for 36 stars, and the SALT [Fe/H] values were used in the fit when available. The remaining [Fe/H] values are from Fabrizio et al. (2019). Since we found a −0.14 dex offset between our [Fe/H] values and the HRS [Fe/H] values collected in Fabrizio et al. (2019), an offset of −0.14 dex was applied to the Fabrizio et al. (2019) [Fe/H] values before the fit was performed. The inclusion of this −0.14 dex offset did not have a significant impact on our fit results.

Reddenings were determined from the 3D maps from Green et al. (2019) as the first choice, or Lallement et al. (2019). As a test of the reddenings derived from the 3D maps, these reddenings were compared to the 2D reddenings from Schlegel, Finkbeiner & Davis (1998). The mean difference in $E(B-V)$ is 0.03 mag with a median of 0.01 mag. In general, the 3D reddenings are less than the 2D reddenings when close to the galactic plane. There are only three stars near the galactic plane whose 3D reddenings are slightly larger than the 2D values, but the difference for all three stars is less than 0.01 mag in $E(B-V)$. Conversion from $E(B-V)$ to extinction assumed $R_v = 3.1$, $A_{W1}/A_v = 0.061$, and $A_{W2}/A_v = 0.048$. The overall properties of these stars used to determine *PLZ* relations are shown in Fig. 10. The reddening plot in the top right shows that most stars in this sample have relatively low reddenings, with $E(B-V) < 0.2$, which corresponds to $A_{W1} < 0.038$. Thus, uncertainties in the reddening values will not significantly impact the *PLZ* fit.

A *PLZ* fit with the *W*1 magnitudes yields

$$M_{W1} = (-2.70 \pm 0.12)(\log P + 0.27) + (0.123 \pm 0.017)([\mathrm{Fe/H}] + 1.3) - (0.390 \pm 0.009)\,. \quad (2)$$

Table 4. Data used to derive our *PLZ* and *PWZ* fits. RRc stars have had their period fundamentalized by adding 0.127 to log *P*. Parallaxes are from *Gaia* EDR3 (Lindegren et al. 2020b); no zero-point correction has been applied. Parallax uncertainties have been increased as discussed in the text. Full table available as supplementary material.

Gaia EDR3 ID	ϖ (mas)	σ_{ϖ} (mas)	*W*1 (mag)	σ_{W1} (mag)	*W*2 (mag)	σ_{W2} (mag)	*V* (mag)	σ_V (mag)	log *P* (d)	$E(B-V)$	[Fe/H] (dex)	$\sigma_{[Fe/H]}$ (dex)
3111925220109675136	0.8718	0.0248	10.2369	0.0064	10.2590	0.0065	11.5276	0.0252	−0.322 095	0.120	−0.60	0.13
5360400630327427072	0.8308	0.0217	9.9791	0.0051	9.9927	0.0050	11.3856	0.0140	−0.277 834	0.319	−1.60	0.13
3604450388616968576	0.6857	0.0359	10.0916	0.0057	10.1043	0.0055	11.4926	0.0096	−0.211 066	0.140	−1.60	0.13
3677686044939929728	0.7579	0.0561	10.2009	0.0062	10.2126	0.0064	11.3491	0.0195	−0.279 211	0.112	−2.20	0.13

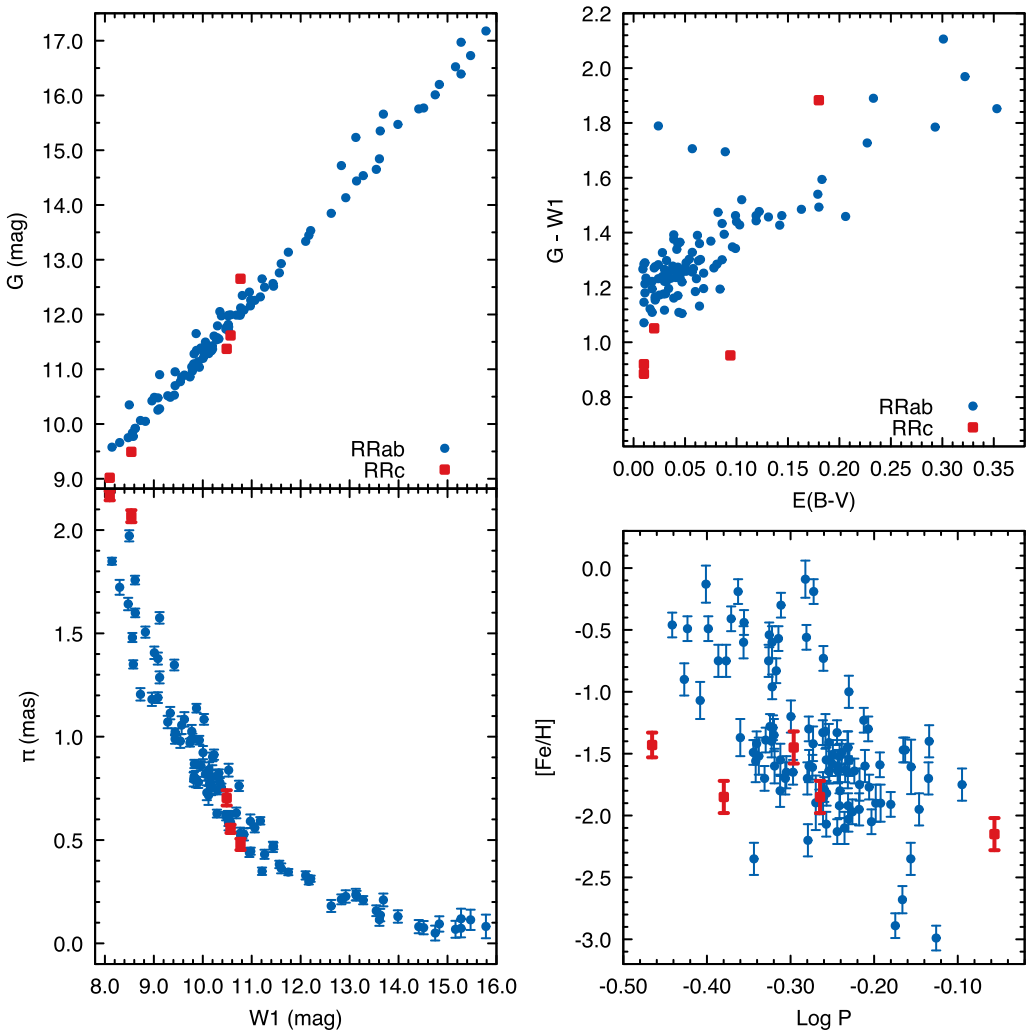

Figure 10. The photometric and parallax properties of the 108 stars used in the *PLZ* fits (left-hand panel), along with their colour–reddening, log Period–[Fe/H] distributions (right-hand panel). RRc stars have had their periods fundamentalized by adding 0.127 to log P_{FO}. *G* magnitudes are from *Gaia* (Riello et al. 2020).

The quality of the fit is good, with a mean absolute normalized deviation of 0.82, where a value of 0.80 is expected for Gaussian uncertainties. The fit is shown visually in Fig. 11.

The explicit *PLZ* fit depends critically on the EDR3 parallaxes, and calibration of the *Gaia* EDR3 parallax zero-point error given by Lindegren et al. (2020a). However Lindegren et al. (2020a) caution that their calibration is tentative and should be used with caution. The primary calibration of the zero-point error is based upon quasars that are numerous at fainter magnitudes, while at brighter magnitudes various secondary sources were used in the calibration. In general, our stars are relatively bright, with 78 per cent of the sample having $G < 13$. The catalogue validation carried out by the *Gaia* team (Fabricius et al. 2020) found that the parallax correction significantly improved the agreement with external data, except for the brighter stars (the LMC and SMC radial velocity samples that have median magnitudes of $\langle G \rangle = 12.8$ and $\langle G \rangle = 12.5$, respectively).

To see what impact errors in the zero-point correction can have our *PLZ* fit, we elected to perform an implicit fit, which solves for a global EDR3 parallax zero-point error as part of the fitting procedure:

$$f \equiv 10^{0.2[a([\mathrm{Fe/H}]+1.3)+b(\log P+0.27)+c]} - (\varpi + \beta)10^{0.2m_{W1,o}-2} = 0, \quad (3)$$

where $\beta = \pi_{zp}$ is determined as part of the fitting process. Since our RR Lyrae sample is distributed randomly on the sky, and solving for a global zero-point error may be appropriate, even though EDR3

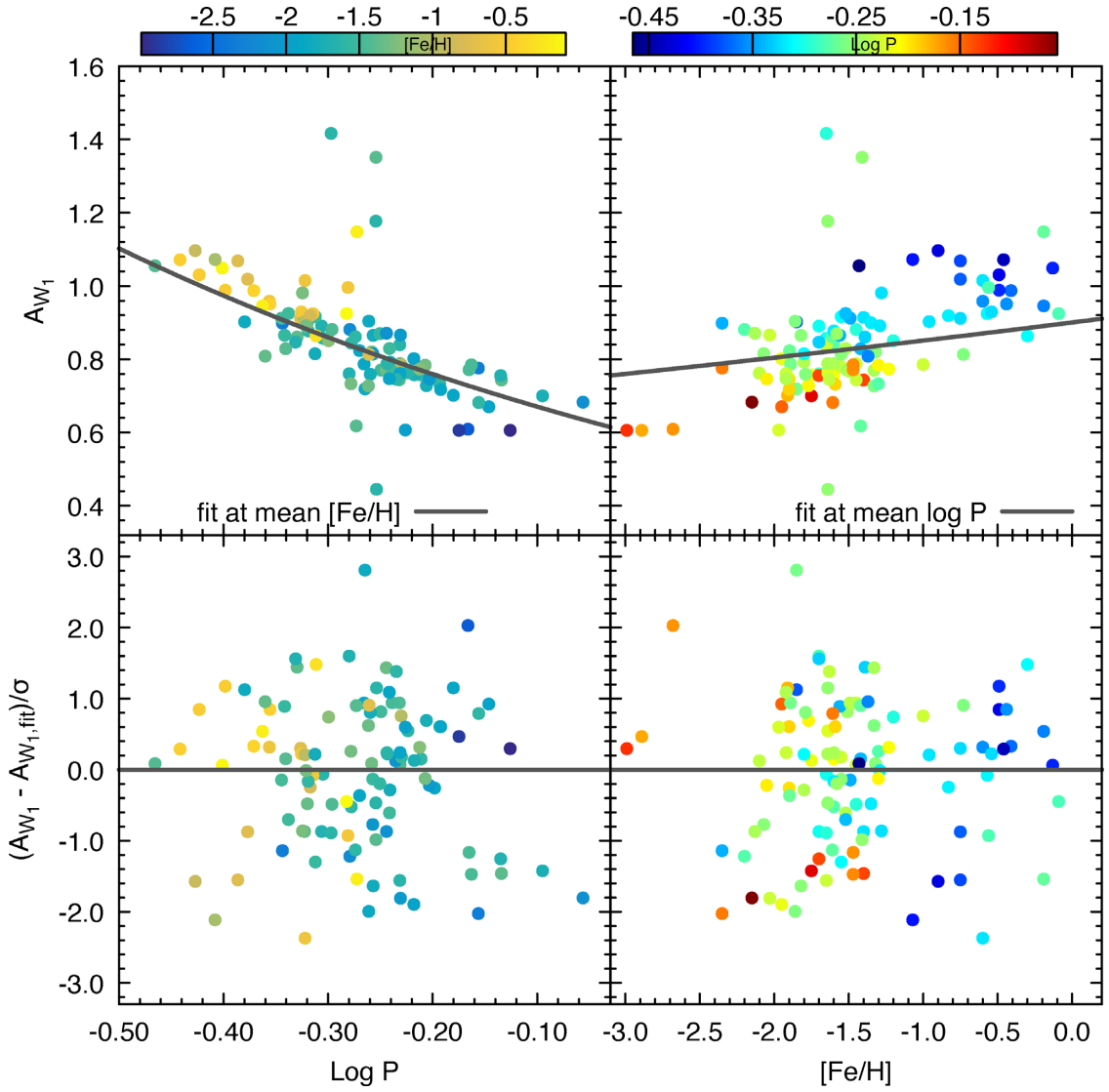

Figure 11. The explicit *P*–*W*1–*Z* fit for the 108 star astrometrically clean sample. Note that A_{W1} is not the absolute magnitude in the *W*1 filter, but comes from the ABL formalism and is defined as $A_{W1} = \varpi 10^{0.2 m_{W1,o}-2}$. Uncertainties A_{W1} (top panels) are not shown to make the figure clear, but can be inferred by looking at the normalized fit residuals that are shown in the bottom panels. Points are coloured by their [Fe/H] values in the left-hand panels, and their log *P* values in the right-hand panels.

parallax zero-point error is known to vary spatially (Lindegren et al. 2020a).

A two-step procedure was utilized when performing the fit. First, as in Layden et al. (2019), equation (3) was fit using an a implicit, non-linear, weighted orthogonal distance approach using ODRPACK95 (Zwolak, Boggs & Watson 2007). This implicit fit accurately determines the *PLZ* zero-point and the DR2 global parallax offset, but Monte Carlo tests (see Layden et al. 2019) indicated that the slopes returned by the implicit fit were biased. Hence, after performing the implicit fit, the derived EDR3 parallax zero-point error was adopted and used in an explicit non-linear fit using R (R Core Team 2018) and its non-linear fitting function `nls` to determine the slopes (*a* and *b* in equation 3). Both of these fitting routines take into account the uncertainties in the observed quantities when determining the fit.

To verify the fitting procedure, five Monte Carlo tests were conducted. In this test, fake data were generated from a known *PLZ* relation, where the distributions (in period, [Fe/H], apparent magnitude, parallax uncertainties, etc.) in the simulated data were drawn from the observed distributions. The simulated data sets include the correlation between period and [Fe/H] which is present in our actual data. These five simulated data sets, with known *PLZ* relations were then run through the exact same fitting routines as were used with our observed data. These simulated data sets had a range of *PLZ* slopes and zero-points, and a range of *Gaia* zero-point errors. These simulations determined that the fitting routines are able to accurately recover the input *PLZ* relation and *Gaia* zero-point error. The average difference between the input coefficients and the fitted coefficients was zero for the two zero-points and the [Fe/H] slope. There is a slight tendency for the fitting routines to find a log period slope which differs by ∼0.02 from the true slope. However, this difference is much smaller than the typical fit error (∼0.16) so we do not regard this disagreement as significant. The standard deviation of the fitted parameters in the Monte Carlo tests was very similar to the average error found by the fitting routines, indicating that the fitting routines are doing a reasonable job of estimating the uncertainty in the fitted coefficients.

An implicit *P*–*W*1–[Fe/H] fit that uses the zero-point corrected EDR3 parallaxes yields

$$M_{W1} = (-2.77 \pm 0.12)(\log P + 0.27) + (0.119 \pm 0.016)([\mathrm{Fe/H}] + 1.3) - (0.421 \pm 0.017) \quad (4)$$

with a global EDR3 parallax offset error of $+0.010 \pm 0.007$ mas. Compared to the explicit fit, the slopes are similar (with differences less than 1σ) while the zero-point of the *PLZ* relation is fainter by 0.03 mag, which is a 1.6σ difference. In these implicit fits, there is a strong correlation between the zero-point in the *PLZ* relation and the *Gaia* EDR3 global parallax offset error.

An implicit *P*–*W*1–[Fe/H] fit that did NOT use the EDR3 parallax zero-point correction was also performed and found

$$M_{W1} = (-2.79 \pm 0.11)(\log P + 0.27) + (0.109 \pm 0.016)([\mathrm{Fe/H}] + 1.3) - (0.419 \pm 0.016) \quad (5)$$

with a global EDR3 parallax offset error of -0.020 ± 0.006 mas. It is interesting to note that the sign of the parallax offset error has changed. These implicit determinations of the EDR3 parallax offset error are consistent with the external catalogue validation done by the *Gaia* team, which found a negative parallax offset error prior to the zero-point correction for all samples (Fabricius et al. 2020). The apparent magnitudes of our sample are most similar to the bright LMC star external catalogue, and Fabricius et al. (2020) found a positive parallax offset error after the zero-point correction was applied (see table 1 in Fabricius et al. 2020). The implicit *PLZ* fit finds also leads to a positive parallax offset error after the zero-point correction is applied. This suggests that the tentative parallax offset correction given by Lindegren et al. (2020a) may be too large for our sample of bright stars.

Looking at the global EDR3 parallax offset error that was found by the implicit fits with (0.010 mas), and without (−0.020 mas) the parallax zero-point correction from Lindegren et al. (2020a), one can estimate that if the zero-point correction is multiplied by 0.65, then the implicit fits would not find a global EDR3 parallax offset error. Accordingly, the zero-point correction for each star was multiplied by 0.65 and new fits were performed. As expected, the implicit fit yields a EDR3 parallax offset error of 0.000 ± 0.006 mas. The implicit fit yields a *PLZ* relation which is very consistent with the explicit fit

$$M_{W1} = (-2.78 \pm 0.12)(\log P + 0.27) + (0.115 \pm 0.016)([\mathrm{Fe/H}] + 1.3) - (0.417 \pm 0.009)\,. \quad (6)$$

The quality of this fit is very good, with a mean absolute normalized deviation of 0.81, an inspection of the residuals shows no trends, while a quantile–quantile plot indicates the residuals follow the expected Gaussian distribution. Given the tentative nature of the EDR3 parallax correction presented by Lindegren et al. (2020a), the above fit is the most reliable estimate of the *P*–*W*1–[Fe/H] relation for our data set. However, the uncertainties in equation (5) do not take into account the uncertainty associated with the EDR3 parallax zero-point error and underestimates the possible error in the *PLZ* zero-point. Given the different zero-points found in the various fits (equations 2–6), our best estimate for the *P*–*W*1–[Fe/H] relation is given by equation (6).

Using the same approach for the *W*2 magnitudes, one finds

$$M_{W2} = (-2.80 \pm 0.12)(\log P + 0.27) + (0.117 \pm 0.016)([\mathrm{Fe/H}] + 1.3) - (0.402 \pm 0.02)\,. \quad (7)$$

The quality of this fit is good, with a mean absolute normalized deviation of 0.82, no residual trends, and the residuals follow the expected Gaussian distribution.

Wesenheit magnitudes are commonly used to derive RR Lyrae *PLZ* relationships since these magnitudes do not rely on knowing the reddening of the individual stars (Madore 1982). We define the Wesenheit magnitude using *V* and *W*1. We use the analytical form of the reddening law from Cardelli, Clayton & Mathis (1989) and the extinctions for the WISE bands from Yuan, Liu & Xiang (2013):

$$W(W1, V - W1) = W1 - 0.065(V - W1)\,.$$

and we find

$$M_{(W1,V-W1)} = (-2.83 \pm 0.10)(\log P + 0.27) + (0.123 \pm 0.014)([\mathrm{Fe/H}] + 1.3) - (0.492 \pm 0.02). \quad (8)$$

The quality of this fit is reasonable, with a mean absolute normalized deviation of 0.85, no residual trends, and the residuals follow the expected Gaussian distribution. We can also use *W*2 instead of *W*1 to form a Wesenheit magnitude with the following relation:

$$W(W2, V - W2) = W2 - 0.050(W2, V - W2)$$

and we find

$$M_{(W2,V-W2)} = (-2.84 \pm 0.10)(\log P + 0.27) + (0.126 \pm 0.014)([\mathrm{Fe/H}] + 1.3) - (0.460 \pm 0.02). \quad (9)$$

The quality of this fit is reasonable, with a mean absolute normalized deviation of 0.87, no residual trends, and the residuals follow the expected Gaussian distribution. A summary of our *PLZ* relations is presented in Table 5.

5.1 Comparison to previous work

A number of other studies have determined *PLZ* relationships in infrared filters. Table 6 shows a collection of previous *PLZ* and *PWZ* relations. Fig. 12 shows our relationship plotted against each of the relations for the *W*1 band while Fig. 13 shows the relations for the *W*2 band. It is clear that most of the differences between the relations occur with the more metal-poor and shorter period RR Lyrae.

Dambis, Rastorguev & Zabolotskikh (2014) collected WISE photometry from 15 Galactic globular clusters to use as calibrating stars. These clusters have known metallicities that are then applied to their member RR Lyrae. They also use Dambis et al. (2013) which uses a homogenized values of period, extinction, metallicity, and average magnitudes in optical and infrared passbands including *W*1. However, even though the catalogue is homogenized, it is not homogeneous. The metallicity measurements come from both HRS and the ΔS method which is from low-resolution spectra. The zero-point (*c*) of the *PLZ* is close to what is found in the other works and our zero-point. The period and metallicity slopes (*a* and *b*) that Dambis et al. (2014) found are the shallowest of all the relations.

Neeley et al. (2017) created theoretical *PLZ* relationships in a variety of optical, near-infrared, and mid-infrared filters using models of RR Lyrae. They use time-dependent convective hydrodynamical models with two different atmosphere models. Their models have a wide metallicity range ([Fe/H] ~ -2.25 to $+0.05$ dex). The relations they derive are tested against Galactic and M4 RR Lyrae from Neeley et al. (2015) and find consistent distances derived from other techniques.

Sesar et al. (2017) used the *Tycho–Gaia* Astrometric Solution (TGAS) along with WISE *W*1 and *W*2 measurements to create their *PLZ* relations. This work uses photometry of 100 RRab stars (no RRc) in *W*1 and *W*2 along with TGAS parallaxes.

Table 5. *PLZ* and *PWZ* relationship coefficients defined as $M = a(\log P + 0.27) + b([\mathrm{Fe/H}] + 1.3) + c$. α is the colour coefficient used in defining a Wesenheit magnitude.

Filter	α[a]	a	b	c
		PLZ		
$W1$		-2.78 ± 0.12	0.115 ± 0.016	-0.417 ± 0.020
$W2$		-2.80 ± 0.12	0.117 ± 0.016	-0.402 ± 0.020
		PWZ		
$W(W1, V - W1)$	0.065	-2.83 ± 0.10	0.123 ± 0.014	-0.492 ± 0.020
$W(W2, V - W2)$	0.050	-2.84 ± 0.10	0.126 ± 0.014	-0.460 ± 0.020

[a]Only used for Wesenheit magnitudes.

Table 6. *PLZ* and *PWZ* relationship slopes defined as $M = a\log P + b[\mathrm{Fe/H}] + c$.

Filter	Source	a	b	c
		PLZ		
$W1$	Dambis et al. (2014)	-2.381 ± 0.097	0.096 ± 0.021	-0.829 ± 0.093
	Neeley et al. (2017)	-2.247 ± 0.018	0.180 ± 0.003	-0.790 ± 0.007
	Sesar et al. (2017)	$-2.470^{+0.74}_{-0.73}$	$0.150^{+0.09}_{-0.08}$	$-0.890^{+0.12}_{-0.10}$
	Muraveva et al. (2018b)	$-2.450^{+0.88}_{-0.82}$	0.16 ± 0.10	$-0.910^{+0.36}_{-0.34}$
[3.6]	Neeley et al. (2019)	-2.40 ± 0.27	0.18 ± 0.03	-0.793 ± 0.007
$W2$	Dambis et al. (2014)	-2.269 ± 0.127	0.108 ± 0.077	-0.776 ± 0.093
	Neeley et al. (2017)	-2.237 ± 0.018	0.185 ± 0.003	-0.785 ± 0.007
	Sesar et al. (2017)	$-2.400^{+0.84}_{-0.82}$	$0.170^{+0.10}_{-0.09}$	$-0.947^{+0.11}_{-0.10}$
[4.5]	Neeley et al. (2019)	-2.45 ± 0.28	0.18 ± 0.03	-0.785 ± 0.007
		PWZ		
$W([3.6], V - [3.6])$	Neeley et al. (2019)	-2.55 ± 0.27	0.18 ± 0.03	-0.46 ± 0.02

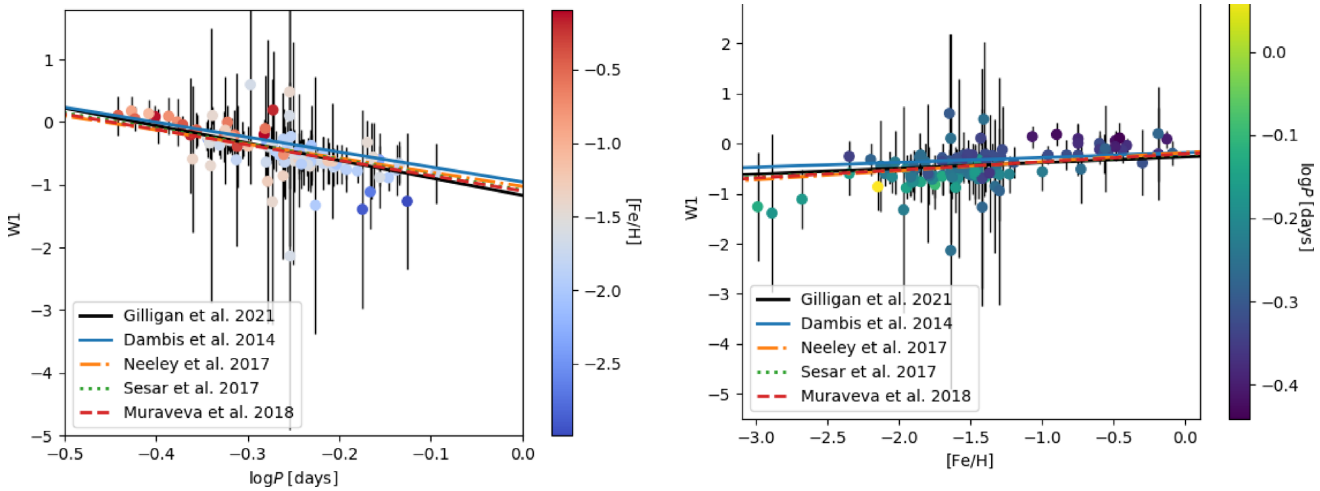

Figure 12. *P*–*W*1–*Z* fits for the full HRS sample compared to the fits from Dambis et al. (2014), Neeley et al. (2017), Sesar et al. (2017), and Muraveva et al. (2018b). The left-hand panel is the absolute magnitude of *W*1 versus log *P*. The second panel is the absolute magnitude versus [Fe/H].

Muraveva et al. (2018b) used *Gaia* DR2 parallaxes and single-epoch WISE *W*1 data in their analysis of 397 stars. This work also uses the catalogue from Dambis et al. (2013), a non-homogeneous sample of RR Lyrae. There are 23 stars in their sample that have their metallicities derived from HRS. They determined the *Gaia* DR2 global zero-point parallax error as part of their fitting procedure.

Neeley et al. (2019) used photometry from The Carnegie RR Lyrae programme and parallaxes from *Gaia* DR2 to determine *PLZ* and *PWZ* relationships to ∼50 Galactic RR Lyrae stars. They use HRS abundances from Fernley & Barnes (1997). This is the only other sample that combines *Gaia* DR2 parallaxes and homogeneous HRS abundances, although they did not determine the *Gaia* DR2 global zero-point parallax error as part of their fitting procedure.

These previous results typically included RRc stars in their analysis, with their periods fundamentalized in the same manner as was performed in our fits. Compared to other studies our log period slope is steeper, while our slope with [Fe/H] is similar. It is not clear what is causing this difference; it could be due to our use of HRS [Fe/H] values, our sample selection/size or the use of EDR3 parallaxes. We note that there are indications from

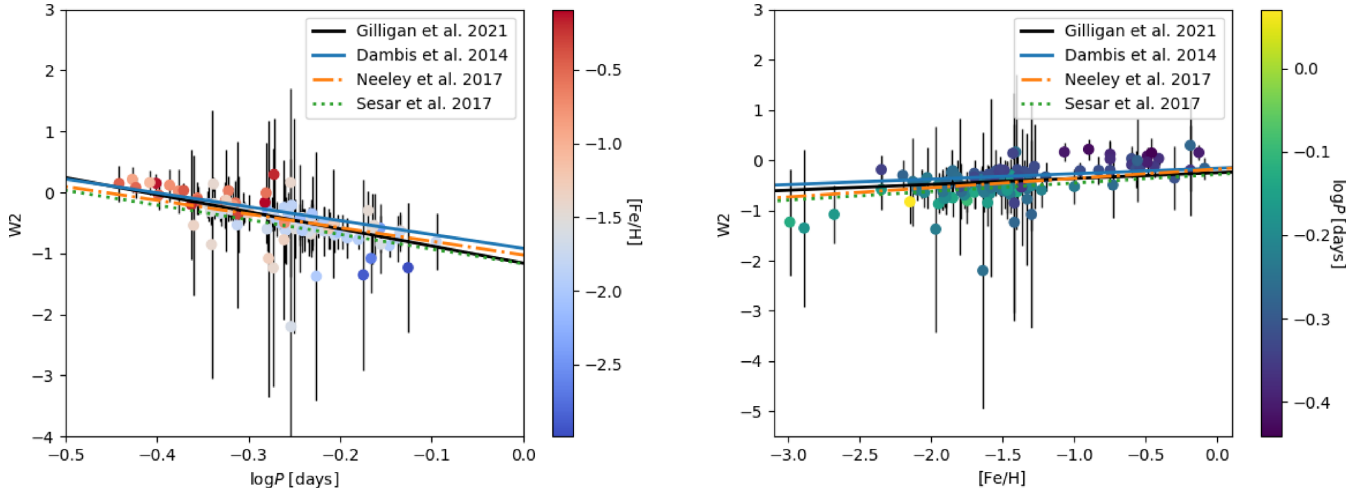

Figure 13. *P–W2–Z* fits for the full HRS sample compared to the fits from Dambis et al. (2014), Neeley et al. (2017), and Sesar et al. (2017). The left-hand panel is the absolute magnitude of *W*2 versus log *P*. The second panel is the absolute magnitude versus [Fe/H].

theoretical models (Neeley et al. 2017) that RRab and RRc stars follow different *PLZ* relations (even when the RRc stars have their periods funamentalized) and so the exact mix of RRab and RRc stars may impact the derived *PLZ* relation. As other studies come out which use the EDR3 parallaxes, it will be interesting to see how their *PLZ* slopes compare to the relations derived in this paper.

A comparison of the *PLZ* zero-point found by different studies is summarized in Table 7. Overall, there is reasonable agreement among the different zero-points. The uncertainty in our zero-point is factor of 7 smaller than the previous best observational determination by Dambis et al. (2014) and our zero-point has the same uncertainty as found in theoretical models by Neeley et al. (2017). Figs 12 and 13 show our fits plotted against various *PW1Z* and *PW2Z* relationships, respectively. In the left-hand panels, we plot with respect to log *P* (at fixed [Fe/H] = −1.3) while for the right-hand panels we plot with respect to [Fe/H] (at fixed log *P* = −0.27). One sees overall, a reasonable agreement between the fits, particularly when taking into account the relatively large zero-point uncertainties that are associated with previous observational determinations.

5.2 Testing the *PLZ* and PWZ relations

To assess the implications of the *PLZ* and PWZ relations listed in Table 5 for distance determinations, we have used them to determine the distance to Reticulum and M4. These two old clusters are optimal targets for testing these relations for two reasons. First, there are available data in the literature for their RR Lyrae stars in the *V* band (Kuehn et al. 2013; Stetson et al. 2014) and in the *Spitzer* IRAC 3.6 and 4.5 μm filters, which are very similar to the *W*1 and *W*2 bands (Neeley et al. 2015; Muraveva et al. 2018a). Secondly, these clusters contain 32 (Demers & Kunkel 1976; Walker 1992) and 47 (Clement et al. 2001; Stetson et al. 2014) RR Lyrae stars, respectively, therefore they are good candidates to test our relations with a statistical significance. To obtain accurate distance moduli, from the 30 RR Lyrae stars of Reticulum with *V*, *W*1, and *W*2 measurements, we reject the same stars that Muraveva et al. (2018a) do not include in their calculations of the PL (i.e. V01, V08, V19, V24, V28, V32) since their position on the colour–magnitude diagram is unusual or they have noisy light curves.

In the case of M4, following Neeley et al. (2015) we reject two stars (V20 and V21) for being blends with nearby sources. Thus, we end up with a set of 31 RR Lyrae stars having *W*1 mean magnitudes and 28 with *W*2 mean magnitudes in M4. In order to obtain the true distance modulus (μ_0) when using the *PLZ* relationships, we correct the *W*1 and *W*2 photometry by reddening. We consider $E(B-V) = 0.03$ (Walker 1992) for Reticulum and $E(B-V) = 0.37$ (Hendricks et al. 2012) for M4. The extinction values for Reticulum ($R_V = 3.1$) are $A_{W1} = 0.203\ E(B-V)$ and $A_{W2} = 0.156\ E(B-V)$ (Monson et al. 2012). For M4, we calculate new absorption coefficients because its ratio of total to selective absorption is different ($R_V = 3.62$, Hendricks et al. 2012). From Cardelli et al. (1989), we obtain $A_K/A_V = 0.124$ for $R_V = 3.62$ and using the $A_{W1}/A_K = 0.56$ and $A_{W2}/A_K = 0.43$ (Indebetouw et al. 2005), we get the following extinction values, $A_{W1} = 0.251\ E(B-V)$ and $A_{W2} = 0.193\ E(B-V)$. It is worth noting that that the α^* coefficients for the Wesenheit magnitudes in M4 were also calculated accordingly to the latter extinction coefficients [i.e. $\alpha^*(W1, V-W1) = 0.075$ and $\alpha^*(W2, V-W2) = 0.056$]. From our final selected sample of RR Lyrae stars, we obtain the distance moduli listed in Table 8, adopting [Fe/H] = −1.66 dex (Mackey & Gilmore 2004) as metallicity value for Reticulum and [Fe/H] = −1.10 dex (see Braga et al. 2015) for M4.

The systematic uncertainties in the distance moduli (shown in Table 8) are obtained by propagation of errors considering the photometric uncertainties of the mean magnitudes in *V*, *W*1, and *W*2, the uncertainties of the coefficients in the relationships (see Table 5), and uncertainties of 0.2 dex in [Fe/H] and of 0.0001 d in the period (which are basically negligible in the final value of the uncertainties). In the case of the *PLZ*, we also take account of the uncertainty that comes from the reddening value, usually considered to be the 10 per cent of its value. The random uncertainty in our distance moduli, estimated from the standard error of the mean (the standard deviation divided by the square root of the number of RR Lyrae stars used to estimate the distance modulus) is quite small in all cases ±0.01 to ±0.02 mag.

Overall, the distance moduli obtained with the different *PLZ* and PWZ relationships of Table 5 are identical for Reticulum and quite similar for M4. Table 8 also contains a selection of distance estimates to these two clusters that have appeared in the literature since 2010. Most of these previous distance determinations are based upon RR Lyr stars, and these studies typically use the cluster RR Lyr stars to find a log *P* slope for the *PLZ* relation, and a calibration of the *PLZ* zero-point based upon theoretical models,

Table 7. Comparison of zero-points. We set $\log P = -0.27$ and [Fe/H] $= -1.3$. For all of the previous studies, we are within 1σ.

Filter	Source	Zero-point
	PLZ	
*W*1	This work	-0.42 ± 0.02
	Dambis et al. (2014)	-0.31 ± 0.14
	Neeley et al. (2017)	-0.42 ± 0.02
	Sesar et al. (2017)	-0.47 ± 0.80
	Muraveva et al. (2018b)	-0.44 ± 0.37
[3.6]	Neeley et al. (2019)	-0.38 ± 0.27
*W*2	This work	-0.40 ± 0.02
	Dambis et al. (2014)	-0.30 ± 0.18
	Neeley et al. (2017)	-0.42 ± 0.02
	Sesar et al. (2017)	-0.52 ± 0.84
[4.5]	Neeley et al. (2019)	-0.36 ± 0.28

Table 8. True distance moduli for Reticulum and M4 from our *PLZ* and PWZ relations (see Table 5) and distance moduli from the literature.

Method	Filter	μ_0 (mag)	Reference
	Reticulum		
RR Lyr EDR3 calib.	$PW(W1, V-W1)$	18.27 ± 0.10	This work
RR Lyr EDR3 calib.	$PW(W2, V-W2)$	18.27 ± 0.10	This work
RR Lyr EDR3 calib.	*W*1	18.27 ± 0.11	This work
RR Lyr EDR3 calib.	*W*2	18.27 ± 0.13	This work
RR Lyr *HST* calib.	*V*	18.40 ± 0.20	Kuehn et al. (2013)
RR Lyr theoretical calib.	*I*	18.47 ± 0.06	Kuehn et al. (2013)
RR Lyr *HST* calib.	*W*1	18.43 ± 0.06	Muraveva et al. (2018a)
RR Lyr TGAS calib.	*W*1	18.33 ± 0.06	Muraveva et al. (2018a)
RR Lyr DR2 calib.	*W*1	18.32 ± 0.06	Muraveva et al. (2018a)
RR Lyr *HST* calib.	*W*2	18.43 ± 0.08	Muraveva et al. (2018a)
RR Lyr TGAS calib.	*W*2	18.34 ± 0.08	Muraveva et al. (2018a)
RR Lyr DR2 calib.	*W*2	18.34 ± 0.08	Muraveva et al. (2018a)
RR Lyr theoretical calib.	*I*	18.51 ± 0.07	Braga et al. (2019)
RR Lyr theoretical calib.	*J*	$18.47? \pm 0.10$	Braga et al. (2019)
RR Lyr theoretical calib.	*K*	$18.49? \pm 0.09$	Braga et al. (2019)
RR Lyr theoretical calib.	*W*1	18.30 ± 0.06	Braga et al. (2019)
RR Lyr theoretical calib.	*W*2	18.31 ± 0.08	Braga et al. (2019)
RR Lyr theoretical calib.	$PW(V, B-I)$	18.52 ± 0.03	Braga et al. (2019)
	M4		
RR Lyr EDR3 calib.	$PW(W1, V-W1)$	11.21 ± 0.08	This work
RR Lyr EDR3 calib.	$PW(W2, V-W2)$	11.17 ± 0.08	This work
RR Lyr EDR3 calib.	*W*1	11.24 ± 0.09	This work
RR Lyr EDR3 calib.	*W*2	11.19 ± 0.09	This work
ZAHB	*V*	11.28 ± 0.06	Hendricks et al. (2012)
Ecl. binaries	—	11.30 ± 0.05	Kaluzny et al. (2013)
RR Lyr *HST* calib.	*W*1	11.41 ± 0.08	Neeley et al. (2015)
RR Lyr *HST* calib.	*W*2	11.39 ± 0.08	Neeley et al. (2015)
RR Lyr theoretical calib.	*R*	11.32 ± 0.11	Braga et al. (2015)
RR Lyr theoretical calib.	*K*	11.30 ± 0.04	Braga et al. (2015)
RR Lyr theoretical calib.	$PW(K, V-K)$	11.28 ± 0.05	Braga et al. (2015)
RR Lyr theoretical calib.	*R* to *K*	11.27 ± 0.02	Braga et al. (2015)
DR2 astrometry	—	11.38 ± 0.10	Gaia Collaboration (2018b)
Red giant oscillations	—	11.26 ± 0.06	Miglio et al. (2016)
DR2 astrometry	—	11.38 ± 0.10	Shao & Li (2019)
RR Lyr DR2 calib.	*I* to *W*2	11.29 ± 0.02	Neeley et al. (2019)

or parallaxes [from either *HST* which obtained parallaxes of five stars, the TGAS, or *Gaia* DR2]. The first column in Table 8 lists what method was used to determine the distance; if it based upon RR Lyr stars then how the zero-point of the *PLZ* relation was calibrated is also listed. The uncertainties listed in Table 8 are those listed by the original authors, which in some cases (such as Muraveva et al. 2018a) are just the random uncertainties, and do not include uncertainties in the *PLZ* zero-point calibration. Braga et al. (2015) provide a large number of distance estimates to M4 (all based upon a theoretical calibration of an RR Lyr *PLZ*) in a range filters,

and only a small sample of their distance estimates are shown in Table 8.

Modern estimates of the distance to Reticulum have all been obtained using RR Lyr stars. The distances determined in this paper are lower than previous estimates, but agree within the uncertainties with determinations which used mid-IR data (*W*1, *W*2). The mid-IR distances are consistently smaller than those obtained at optical wavelengths, though the differences are not large. For example, our distance differs by 2.4 σ from the largest distance in Table 8 from Braga et al. (2019) which is based upon a Wesenheit relation using *V*, *B*, and *I*. We note that the distance determination depends somewhat on the assumed cluster reddening (for *PLZ* relations) and [Fe/H] value, and different authors have used slightly different values, for example Braga et al. (2019) used [Fe/H] = −1.70.

Averaging together the distance determinations to the globular cluster M4 found in this paper leads to $\mu_o = 11.21 \pm 0.09$ mag. M4 has a relatively large [E ($B - V$) = 0.37] and variable reddening with a non-standard extinction law (Hendricks et al. 2012). The uncertainties introduced by this reddening are minimized in our mid-IR and Wesenheit distance determinations. In addition to RR Lyr based determinations, previous work has determined the distance to M4 from theoretical zero-age horizontal branch (ZAHB) models, eclipsing binaries, solar-like oscillations in red giant stars, and *Gaia* DR2 astrometry of the brighter stars in M4. The distances found in this work are once again shorter than previous distance determinations, though the differences are not large. In their paper on determining distances to globular clusters, Gaia Collaboration (2018b) note that there was a systematic difference of −0.029 mas in their parallaxes as compared to the 2010 web update of the catalogue of globular cluster properties by Harris (1996), and that the calibration noise is 0.025 mas. Due to other indications of a DR2 parallax offset error of −0.029 mas, the Gaia Collaboration (2018b) distance to M4 shown in Table 8 has been corrected for this offset. The distance determined to M4 in this paper differs by 1.3σ from those found by Gaia Collaboration (2018b).

Reasonable agreement is found with the distances determined with ZAHB models, eclipsing binaries, and solar-like oscillations and many of the previous RR Lyr based determinations. For example, our distance is 0.9σ smaller than the geometric eclipsing binary distance and 0.5σ smaller than the distance determined from analysis of solar-like oscillations in red giant stars.

Based upon the comparisons between distance estimates to M4 and Reticulum, it appears that our mid-IR calibration of the RR Lyr *PLZ* relation, which is based upon *Gaia* EDR3 parallaxes and high-dispersion spectroscopic abundances, yields distances which agrees within the uncertainties with other distance determinations. However, our distances are consistently smaller by ∼ 5–10 per cent compared to previous determinations. It will be interesting to see how our distance scale compares to other EDR3 distance estimates in the future.

6 CONCLUSION

We performed a homogeneous spectral analysis of 49 RR Lyrae stars. This increases the number of RR Lyrae stars with HRS metallicity determination from 109 (Fabrizio et al. 2019) to 147. Our average error in our [Fe/H] determinations is 0.15 dex. We are able to compare our sample to results from three different methods, finding agreement between our overlapping stars. With these newly measured metallicities and data from Mullen et al. (2020), we find new *PLZ* relationships in the mid-IR using *Gaia* EDR3 parallaxes. These *PLZ* relations are summarized in Table 5 and have substantially smaller uncertainties than previous observational determinations of the RR Lyr *PLZ* relations in the mid-IR.

This work will be extremely useful in Dall'Ora et al. (in preparation) that will examine near-infrared (*JHK*) light curves for all of the RR Lyrae examined here and many more. The sample of stars with both accurate light curves and metallicity determinations will form the backbone of an independent *PLZ* relationship that can be used for further rungs of the distance ladder.

ACKNOWLEDGEMENTS

The spectroscopic observations reported in this paper were obtained with the Southern African Large Telescope (SALT). This work has made use of data from the European Space Agency (ESA) mission *Gaia* (https://www.cosmos.esa.int/gaia), processed by the *Gaia* Data Processing and Analysis Consortium (DPAC, https://www.cosmos.esa.int/web/gaia/dpac/consortium). Funding for the DPAC has been provided by national institutions, in particular the institutions participating in the *Gaia* Multilateral Agreement. This publication makes use of data products from WISE, which is a joint project of the University of California, Los Angeles, and the Jet Propulsion Laboratory (JPL)/California Institute of Technology (Caltech), funded by the National Aeronautics and Space Administration (NASA), and from NEOWISE, which is a JPL/Caltech project funded by NASA's Planetary Science Division. MM and JPM were partially supported by the National Science Foundation under Grant No. AST-1714534. CS acknowledges support from NSF Grant AST1616040.

DATA AVAILABILITY

The data (reduced spectra) can be found from SALT at https://ssda.saao.ac.za/. Other data underlying this article will be shared on reasonable request to the corresponding author.

REFERENCES

Arenou F., Luri X., 1999, in Egret D., Heck A., eds, ASP Conf. Ser. Vol. 167, Harmonizing Cosmic Distance Scales in a Post-HIPPARCOS Era. Astron. Soc. Pac., San Francisco, p. 13
Beers T. C., Chiba M., Yoshii Y., Platais I., Hanson R. B., Fuchs B., Rossi S., 2000, AJ, 119, 2866
Benedict G. F. et al., 2011, AJ, 142, 187
Bono G., 2003, RR Lyrae Distance Scale: Theory and Observations. Springer, Heidelberg, Germany, p. 85
Braga V. F. et al., 2015, ApJ, 799, 165
Braga V. F. et al., 2018, AJ, 155, 137
Braga V. F. et al., 2019, A&A, 625, A1
Cardelli J. A., Clayton G. C., Mathis J. S., 1989, ApJ, 345, 245
Castelli F., Kurucz R. L., 2003, Modelling of Stellar Atmospheres, Astronomical Society of the Pacific, San Francisco
Catelan M., Pritzl B. J., Smith H. A., 2004, ApJS, 154, 633
Chadid M., Sneden C., Preston G. W., 2017, ApJ, 835, 187
Clement C. M. et al., 2001, AJ, 122, 2587
Crestani J. et al., 2021, submitted
Dambis A. K., Berdnikov L. N., Kniazev A. Y., Kravtsov V. V., Rastorguev A. S., Sefako R., Vozyakova O. V., 2013, MNRAS, 435, 3206
Dambis A. K., Rastorguev A. S., Zabolotskikh M. V., 2014, MNRAS, 439, 3765
Demers S., Kunkel W. E., 1976, ApJ, 208, 932
Fabricius C. et al., 2020, preprint (arXiv:2012.06242)
Fabrizio M. et al., 2019, ApJ, 882, 169
Fernley J., Barnes T. G., 1997, A&AS, 125, 313
For B.-Q., Sneden C., Preston G. W., 2011, ApJS, 197, 29

Fossati L., Kolenberg K., Shulyak D. V., Elmasli A., Tsymbal V., Barnes T. G., Guggenberger E., Kochukhov O., 2014, MNRAS, 445, 4094
Gaia Collaboration, 2018a, A&A, 616, A1
Gaia Collaboration, 2018b, A&A, 616, A12
Govea J., Gomez T., Preston G. W., Sneden C., 2014, ApJ, 782, 59
Green G. M., Schlafly E., Zucker C., Speagle J. S., Finkbeiner D., 2019, ApJ, 887, 93
Harris W. E., 1996, AJ, 112, 1487
Hendricks B., Stetson P. B., VandenBerg D. A., Dall'Ora M., 2012, AJ, 144, 25
Indebetouw R. et al., 2005, ApJ, 619, 931
Jayasinghe T. et al., 2018, MNRAS, 477, 3145
Kaluzny J. et al., 2013, AJ, 145, 43
Kniazev A. Y., Gvaramadze V. V., Berdnikov L. N., 2016, MNRAS, 459, 3068
Kniazev A. Y., Gvaramadze V. V., Berdnikov L. N., 2017, in Balega Y. Y., Kudryavtsev D. O., Romanyuk I. I., Yakunin I. A., eds, ASP Conf. Ser. Vol. 510, Stars: From Collapse to Collapse. Astron. Soc. Pac., San Francisco, p. 480
Kuehn C. A. et al., 2013, AJ, 145, 160
Lallement R., Babusiaux C., Vergely J. L., Katz D., Arenou F., Valette B., Hottier C., Capitanio L., 2019, A&A, 625, A135
Layden A. C., 1994, AJ, 108, 1016
Layden A. C., Tiede G. P., Chaboyer B., Bunner C., Smitka M. T., 2019, AJ, 158, 105
Lindegren L. et al., 2020a, preprint (arXiv:2012.01742)
Lindegren L. et al., 2020b, preprint (arXiv:2012.03380)
Liu S., Zhao G., Chen Y.-Q., Takeda Y., Honda S., 2013, Res. Astron. Astrophys., 13, 1307
Longmore A. J., Fernley J. A., Jameson R. F., 1986, MNRAS, 220, 279
Mackey A. D., Gilmore G. F., 2004, MNRAS, 355, 504
Madore B. F., 1982, ApJ, 253, 575
Mainzer A. et al., 2011, ApJ, 731, 53
Marconi M. et al., 2015, ApJ, 808, 50
Miglio A. et al., 2016, MNRAS, 461, 760
Monson A. J., Freedman W. L., Madore B. F., Persson S. E., Scowcroft V., Seibert M., Rigby J. R., 2012, ApJ, 759, 146
Mullen J. et al., 2021, submitted
Muraveva T., Garofalo A., Scowcroft V., Clementini G., Freedman W. L., Madore B. F., Monson A. J., 2018a, MNRAS, 480, 4138
Muraveva T., Delgado H. E., Clementini G., Sarro L. M., Garofalo A., 2018b, MNRAS, 481, 1195
Neeley J. R. et al., 2015, ApJ, 808, 11
Neeley J. R. et al., 2017, ApJ, 841, 84
Neeley J. R. et al., 2019, MNRAS, 490, 4254
Persson S. E., Madore B. F., Krzemiński W., Freedman W. L., Roth M., Murphy D. C., 2004, AJ, 128, 2239
Planck Collaboration VI, 2018, A&A, 641, A6
Preston G. W., 2011, AJ, 141, 6
R Core Team, 2018, R: A Language and Environment for Statistical Computing. R Foundation for Statistical Computing, Vienna, Austria, Available at: https://www.R-project.org/
Riello M. et al., 2020, preprint (arXiv:2012.01916)
Riess A. G., Casertano S., Yuan W., Macri L. M., Scolnic D., 2019, ApJ, 876, 85
Schlegel D. J., Finkbeiner D. P., Davis M., 1998, ApJ, 500, 525
Sesar B., Fouesneau M., Price-Whelan A. M., Bailer-Jones C. A. L., Gould A., Rix H.-W., 2017, ApJ, 838, 107
Shao Z., Li L., 2019, MNRAS, 489, 3093
Shappee B. J. et al., 2014, ApJ, 788, 48
Sneden C., 1973, ApJ, 184, 839
Sobeck J. S. et al., 2011, AJ, 141, 175
Stetson P. B. et al., 2014, PASP, 126, 521
Walker A. R., 1992, AJ, 103, 1166
Wright E. L. et al., 2010, AJ, 140, 1868
Yuan H. B., Liu X. W., Xiang M. S., 2013, MNRAS, 430, 2188
Zwolak J. W., Boggs P. T., Watson L. T., 2007, ACM Trans. Math. Softw., 33, 27

SUPPORTING INFORMATION

Supplementary data are available at *MNRAS* online.

suppl_data

Please note: Oxford University Press is not responsible for the content or functionality of any supporting materials supplied by the authors. Any queries (other than missing material) should be directed to the corresponding author for the article.

This paper has been typeset from a TEX/LATEX file prepared by the author.